Geophysical Research Letters

RESEARCH LETTER
10.1029/2023GL107244

Characteristic Slow-Slip Events on the Superstition Hills Fault, Southern California

Ellis J. Vavra[1], Yuri Fialko[1], Thomas Rockwell[2,3], Roger Bilham[4], Petra Štěpančíková[3], Jakub Stemberk[3], Petr Tábořík[3], and Josef Stemberk[3]

[1]Institute of Geophysics and Planetary Physics, Scripps Institution of Oceanography, University of California, San Diego, CA, USA, [2]Department of Geological Sciences, San Diego State University, San Diego, CA, USA, [3]Institute of Rock Structure and Mechanics, Czech Academy of Sciences, Prague, Czech Republic, [4]Cooperative Institute for Research in Environmental Sciences, University of Colorado, Boulder, CO, USA

Key Points:

- We document a recent spontaneous slow slip event (SSE) on the Superstition Hills Fault using creepmeter, Interferometric Synthetic Aperture Radar, Global Navigation Satellite System, and field measurements
- Over 41 mm of slip occurred from mid-May to mid-July 2023, with moment release corresponding to a M_w 4.5 earthquake
- The kinematics of the 2023 event are remarkably similar to several previous SSEs, suggesting a characteristic rupture process

Supporting Information:

Supporting Information may be found in the online version of this article.

Correspondence to:

E. J. Vavra,
evavra@ucsd.edu

Citation:

Vavra, E. J., Fialko, Y., Rockwell, T., Bilham, R., Štěpančíková, P., Stemberk, J., et al. (2024). Characteristic slow-slip events on the Superstition Hills Fault, Southern California. *Geophysical Research Letters*, *51*, e2023GL107244. https://doi.org/10.1029/2023GL107244

Received 30 NOV 2023
Accepted 9 FEB 2024

Author Contributions:

Conceptualization: Ellis J. Vavra, Yuri Fialko, Thomas Rockwell, Roger Bilham, Petra Štěpančíková
Data curation: Ellis J. Vavra, Yuri Fialko, Thomas Rockwell, Roger Bilham, Petra Štěpančíková, Jakub Stemberk, Petr Tábořík, Josef Stemberk
Formal analysis: Ellis J. Vavra
Funding acquisition: Roger Bilham, Petra Štěpančíková

Abstract The Superstition Hills Fault (SHF) exhibits a rich spectrum of slip modes, including M 6+ earthquakes, afterslip, quasi-steady creep, and both triggered and spontaneous slow slip events (SSEs). Following 13 years of quiescence, creepmeters recorded 25 mm of slip during 16–19 May 2023. Additional sub-events brought the total slip to 41 mm. The event nucleated on the northern SHF in early-May and propagated bi-laterally at rates on the order of kilometers per day. Surface offsets reveal a bi-modal slip distribution, with slip on the northern section of the fault being less localized and lower amplitude compared to the southern section. Kinematic slip models confirm systematic variations in the slip distribution along-strike and with depth and suggest that slip is largely confined to the shallow sedimentary layer. Observations and models of the 2023 SSE bear a strong similarity to previous slip episodes in 1999, 2006, and 2010, suggesting a characteristic behavior.

Plain Language Summary Studying the mechanical properties and behavior of faults is essential for understanding earthquake ruptures. In this study, we investigate a recent slip event on the Superstition Hills Fault (SHF), which has a well-documented record of slip. A notable aspect of the SHF is that it periodically undergoes "slow slip events" (SSEs), where the fault slips and releases energy without any accompanied ground shaking. During May-July 2023, the SHF experienced a major SSE for the first time in 13 years. Our analysis shows that it was the largest documented SSE on the SHF and released equivalent energy to a magnitude 4.5 earthquake. We also find that the spatial pattern of fault slip is very similar to several previous slip events in 1999, 2006, and 2010, suggesting that the SHF has a tendency to slip in a characteristic manner.

1. Introduction

The Superstition Hills Fault (SHF) is located at the southern end of the San Jacinto Fault Zone, 35 km north of the United States-Mexico border in Southern California (e.g., Hudnut & Sieh, 1989; R. V. Sharp, 1967; Tymofyeyeva & Fialko, 2018). The SHF has a well-documented record of time-dependent slip, spanning the coseismic, postseismic, and interseismic phases of the earthquake cycle. Early observations dating back to 1960s detected surface creep along the SHF at an average rate of 0.5 mm/yr (Louie et al., 1985), as well as slow slip events (SSEs; also referred to as creep events) triggered by local earthquakes (Allen et al., 1972; Fuis, 1982; Sharp et al., 1986).

On 24 Nov 1987, the SHF ruptured in a M_S 6.6 earthquake with 1 m of average coseismic slip below 5 km depth (Wald et al., 1990). Significant surface slip was delayed by minutes or hours, but within a day was quantified as rapidly developing afterslip (Sharp et al., 1986; Williams & Magistrale, 1989), that in the following 3 years decayed to low rates, cumulatively matching coseismic slip at depth (Bilham, 1989). Creepmeter observations showed that afterslip included frequent SSEs (e.g., Wei et al., 2013). The rate of decay of afterslip was interpreted in terms of velocity-strengthening behavior of the uppermost 5 km of the fault (Barbot et al., 2009; Marone et al., 1991). Several years later, the 1992 M_w 7.3 Landers and M_w 6.2 Big Bear earthquakes triggered 8+ mm of slip at the site of a creepmeter operated by CU Boulder, and up to 20 mm elsewhere (Bodin et al., 1994; Rymer, 2000). The 1999 M_w 7.1 Hector Mine earthquake triggered surface slip of up to 18 mm along at least 9 km of the SHF (Rymer et al., 2002).

Most of the observed shallow SSEs on the SHF appear to be dynamically triggered by regional (e.g., Allen et al., 1972; Hauksson et al., 2013; Louie et al., 1985; Wei et al., 2011) or teleseismic (Heflin et al., 2020)

Investigation: Ellis J. Vavra, Yuri Fialko, Thomas Rockwell, Roger Bilham, Petra Štěpančíková, Jakub Stemberk, Petr Tábořík, Josef Stemberk
Methodology: Ellis J. Vavra, Yuri Fialko, Thomas Rockwell, Roger Bilham, Petra Štěpančíková, Jakub Stemberk, Petr Tábořík, Josef Stemberk
Project administration: Roger Bilham, Petra Štěpančíková
Resources: Yuri Fialko, Thomas Rockwell, Roger Bilham, Petra Štěpančíková
Software: Ellis J. Vavra, Yuri Fialko
Supervision: Yuri Fialko, Thomas Rockwell, Roger Bilham, Petra Štěpančíková
Validation: Ellis J. Vavra, Yuri Fialko, Roger Bilham, Petra Štěpančíková, Jakub Stemberk, Petr Tábořík
Writing – original draft: Ellis J. Vavra
Writing – review & editing: Ellis J. Vavra, Yuri Fialko, Thomas Rockwell, Roger Bilham, Petra Štěpančíková, Jakub Stemberk, Petr Tábořík, Josef Stemberk

earthquakes. This is similar to the behavior observed on other major faults in the area that exhibit shallow creep, in particular the Southern San Andreas Fault (e.g., Bodin et al., 1994; Fialko, 2006; Tymofyeyeva et al., 2019). However, some shallow SSEs on the SHF occur spontaneously (Wei et al., 2009), analogous to those observed on megathrusts in subduction zones (e.g., Dragert et al., 2001; LaBonte et al., 2009; Wallace, 2020).

The first report of a spontaneous SSE on the SHF documented ∼30 mm of surface slip that occurred in October of 2006 over a time period of two weeks, with most of the slip occurring in the first three days (Wei et al., 2009). Inversions of the ENVISAT Interferometric Synthetic Aperture Radar (InSAR) data capturing the 2006 event showed that the latter was equivalent to a M_w 4.2 earthquake (assuming a shear modulus of 6 GPa; "The SCEC Unified Community Velocity Model Software Framework", 2017) and that slip was largely confined to shallowest 2–3 km of the crust, consistent with the inferred depth of sediments (Kohler & Fuis, 1986; Wei et al., 2009; Williams & Magistrale, 1989).

An SSE with comparable size and slip pattern was triggered by the 2010 M_w 7.2 El Mayor-Cucapah earthquake (Donnellan et al., 2014; Wei et al., 2011). Wei et al. (2015) examined ERS-1/2 InSAR data spanning 1992–2004 (during which no creepmeter measurements were made), and detected at least four more events. The first and second events occurred between November 1993-July 1995, and October-December 1996, respectively, and each produced about 20 mm of slip. The third and fourth events occurred in 1997 and 1998, respectively, but were limited to the northern half of the fault. Additional minor slip on the SHF was triggered by a pair of M_w 5+ earthquakes in the 2012 Brawley Swarm, as well as the teleseismic 2017 M_w 8.2 Chiapas (Mexico) earthquake (Hauksson et al., 2013; Heflin et al., 2020).

In this study, we present observations and models of a new spontaneous SSE which began in May 2023. We show that the latest SSE is the largest observed on the SHF, and that it bears a strong resemblance to previous events (in particular, the spontaneous 2006, as well as the triggered 1999 and 2010 events), suggesting a characteristic rupture pattern.

2. Data and Methods

The 2023 SSE was initially detected by two creepmeters installed on the southern SHF, 700 m northwest of Imler Road (Figure 3). The Colorado (COL) creepmeter records slip at 1-min intervals and consists of a 6-m-long, 4-mm-diameter pultruded carbon rod anchored ±1.5 m from the fault trace (Bilham & Castillo, 2020). The TM71 creepmeter consists of two Moiré-fringe optical sensors arranged to measure strike-slip, dip-slip, and dilation, from which the total displacement vector can be calculated (Klimeš et al., 2012; Košťák, 1969; Martí et al., 2013). TM71 samples at daily intervals and is anchored ±0.5 m on either side of the fault trace. Both instruments recorded an abrupt onset of an SSE on 16 May 2023 (Figure 2a). Additional details on the creepmeters are provided in the Supporting Information.

Similar, albeit smaller-amplitude, slip was registered by continuously-operating GNSS station P503, located ∼3 km northwest of the creepmeters and ∼300 m east from the fault trace (Figure 1). To remove noise due to common-mode regional signals, we computed the change in fault-parallel baseline between station P503 and station P493 (Figures 1 and 2).

The 2023 SSE was also imaged by the European Space Agency's Sentinel-1A synthetic aperture radar satellite. We used data from Sentinel-1A's descending track 173 to map surface deformation associated with the slip episode. Unfortunately, no acquisitions were made from the ascending track covering the area of interest. We used the acquisition from 3 May 2023 as reference and processed interferograms using all data collected between October 2022-November 2023. To suppress atmospheric contributions, which are the dominant source of noise for measuring small-amplitude deformation (e.g., Nof et al., 2012; Pearse & Fialko, 2010; Zebker et al., 1997), we used a Common Scene Stacking method (Tymofyeyeva & Fialko, 2015) to estimate atmospheric phase screens (APS) for 3 May and 26 July acquisitions. To do so, we generated all interferometric pairs with the 3 May end date, and the 26 July start date. We chose pairs that minimize the perpendicular baseline, and are least affected by decorrelation. The resulting subsets were averaged to obtain APS for the respective common scenes. We inspected the estimated APS to ensure that no fault slip occurred outside of the 3 May–26 July 2023 interval, which might bias our deformation measurements, and subtracted the estimated APS from the 3 May to 26 July interferogram (Figure 3). For interferograms that span shorter time periods during the SSE, we only applied the

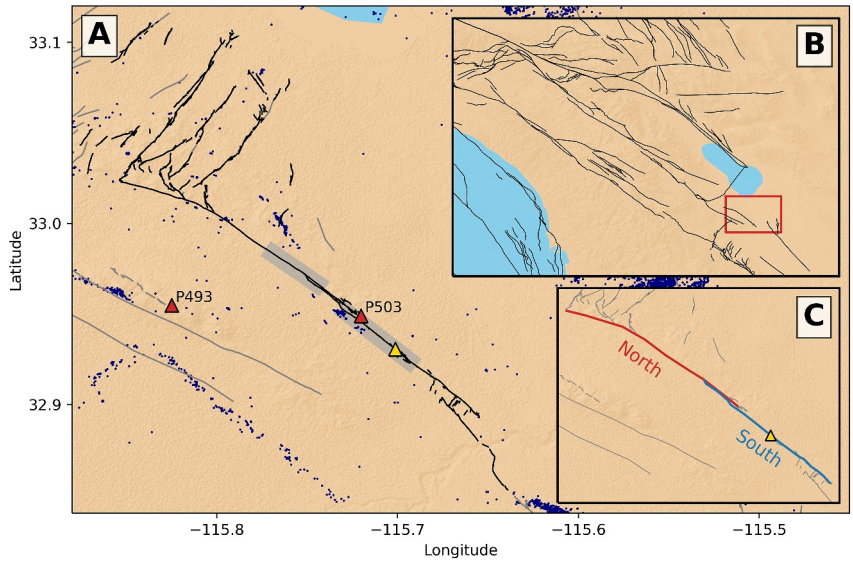

Figure 1. (a) Regional map of the Superstition Hills Fault (SHF). Quaternary faults are shown in gray (USGS, 2020) with the 1987 SHF surface rupture shown in black. The location of the creepmeters is shown with a yellow triangle. Global Navigation Satellite System stations P503 and P493 are shown as red triangles. Gray shading indicates the extent of the field survey. Seismicity from 2008 to 2017 is shown as blue dots (Ross et al., 2019). (b) Regional tectonic setting of the SHF. Major fault traces are plotted in black (Shaw et al., 2015). The area covered by panel (a) is shown in red. (c) The primary fault traces of the northern (red) and southern (blue) strands of the SHF.

correction for the start date (3–15 May, Figure 2b, Figures S1 and S2 in Supporting Information S1; 3 May–8 June, Figure 4 and Figure S3 in Supporting Information S1).

To evaluate slip along the fault trace, we computed offsets from fault-perpendicular swaths at 250 m intervals along the fault. We also computed the maximum observed surface offsets for cases where slip is distributed across a shear zone of finite width, as opposed to localized on the fault trace (Figures S2 and S3 in Supporting Information S1). Further details on the offset estimation procedures can be found in the Supporting Information. Figure 4b shows the along-fault distribution of surface slip measured by InSAR.

We also conducted field surveys to document surface expressions of shallow creep, verify the rupture extent, and measure offsets for comparisons with other data sets. Preliminary field investigations on 20 May 2023 revealed evidence of cracking and centimeter-scale offsets along the fault trace near Imler Road and the creepmeters. A more detailed survey on 11 June 2023 mapped surface cracks and measured their offsets (Figure 4a and Figure S4 in Supporting Information S1) along much of the SHF. The southern section of the SHF produced a localized surface rupture that could be easily traced for several kilometers both north and south of the creepmeters (Figures 1a and 4b). Further to the north, surface expressions of shallow creep become less obvious, likely due to a distributed nature of surface deformation (Figure S3 in Supporting Information S1) and possibly an increased presence of loose sand. Overall, the measured offsets on the northern SHF are smaller than those on the southern SHF (Figure 4b). A ∼3 km stretch north of the fault step-over near the GNSS site P503 (Figure 1a) was not mapped due to logistical constraints.

3. Evolution of Fault Slip During the 2023 SSE

High-rate data from the COL creepmeter recorded the onset of the 2023 SSE on 16 May at 18:29 UTC (11:29 PDT, local time) at the location of the creepmeter (see Figure 2a). Retroactive analysis of 12-day Sentinel-1A interferograms reveals that the SSE likely nucleated sometime between 3 and 15 May 2023 on the northern SHF (Figure 2b, Figure S1 and S2 in Supporting Information S1) and propagated to the south. Investigation of both regional and global seismic catalogs does not reveal potential triggers (see Supporting Information for details), suggesting slip initiated spontaneously. The southernmost extent of slip that occurred between 3 and 15 May 2023 was approximately ∼10 km from the creepmeters (Figure S1 in Supporting Information S1), implying an along-strike rupture velocity on the order of kilometers per day.

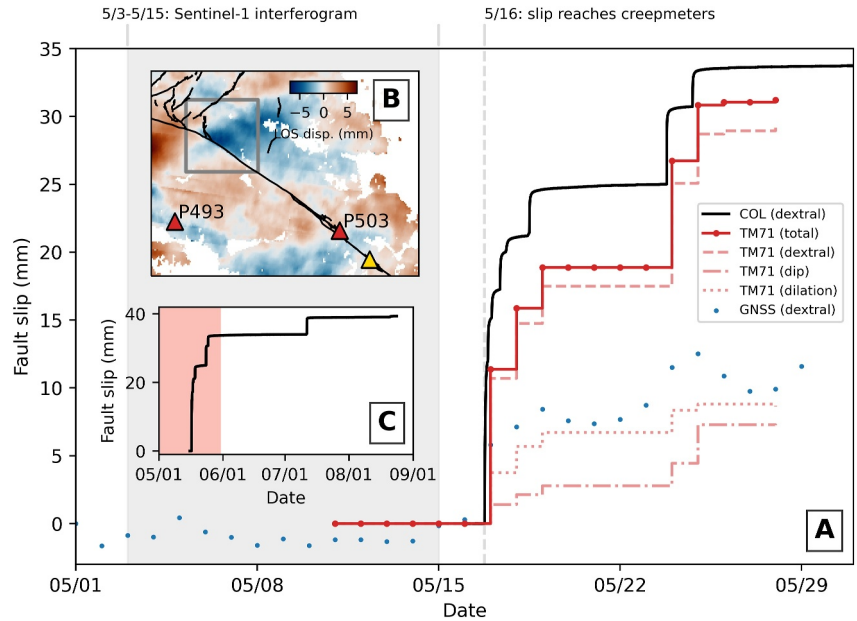

Figure 2. (a) Fault slip during May 2023. Dextral slip measured by COL creepmeter is shown in black. Red lines show dextral slip (dashed), dip slip (dot-dashed), dilation (dotted), and total fault displacement (solid) from TM71 creepmeter. Blue dots show the fault-parallel baseline change between Global Navigation Satellite System stations P503 and P493. Gray shading indicates the epoch of the 3–15 May Sentinel-1 interferogram. (b) 3–15 May Sentinel-1 interferogram showing initial slip on the northern Superstition Hills Fault (gray box). (c) Time series of fault slip through August 2023 from COL. Red shading indicates the time span of time series in panel (a).

Over 20 mm of slip occurred within 24 hr after the slip front reached the creepmeters, and over 80% of slip registered by the creepmeters occurred in first 2 weeks of the event (Figures 2a and 2c). A 5 mm sub-event on 11 July 2023 brought the total amplitude of the SSE to 41 mm near Imler Road (Figure 2c). InSAR data indicate that slip propagated both northwest and southeast along-strike (Figures S2 and S3 in Supporting Information S1), rupturing the entire shallow section of the SHF. The main slip patch is observed within several km of the creepmeters on the southern segment of the SHF, with ∼45 mm of slip accumulating by mid-June 2023 (Figure 4b). Slip on the northern segment (3–15 km northwest of the creepmeters) was on average ∼5 mm, with a small peak 7–8 km north of the creepmeters (Figure 4). However, the InSAR data show that slip on the northern section was distributed across a shear zone 400–1,300 m wide (Figure S3 in Supporting Information S1), so that the maximum fault-parallel displacements occurred away from the fault trace, amounting to 10–20 mm (Figure 4b).

Figure 4b shows a comparison of surface offsets along the SHF measured using different techniques. While the data in general show good agreement, some systematic differences are apparent. In particular, the InSAR-derived offsets are larger compared to the field and creepmeter measurements (the only exception is a ∼30 mm offset suggested by field observations at ∼6 km northwest from the creepmeters, see Figure 4b; this data point may be biased due to erosion of surface cracks in soft sediments). Such differences are expected if fault creep is not perfectly localized on a fault trace. All three observations are collocated near Imler Road and the measured slip increases with the observation aperture (centimeters for field measurements, meters for creepmeters, and hundreds of meters for InSAR).

InSAR data also indicate that slip on the southern section of the SHF occurs in a zone narrower than ∼100 m (Figure S3 in Supporting Information S1), much more localized compared to slip on the northern section. It was suggested that continuous across-fault variations in surface displacements due to fault slip might result from a strong shallow layer resisting the propagation of slip to the Earth's surface, resulting in a "surface locking depth" (Brooks et al., 2017; Parker et al., 2021). However, given the low mechanical strength of near-surface sediments, a more plausible explanation is that the effective width of the shear zone reflects distributed failure within the fault damage zone with depth comparable to (or greater than) its width (Fialko et al., 2002; Lindsey, Fialko, et al., 2014). Comparisons of surface ruptures from InSAR and field surveys for the 2006 and 2010 SSEs reveal a

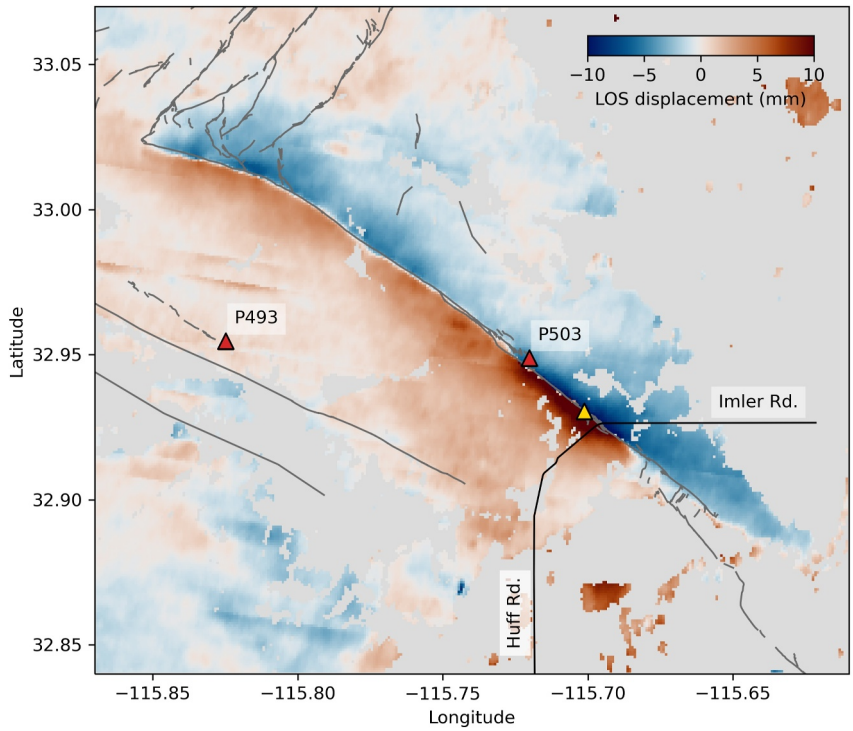

Figure 3. Line of sight displacements due to 2023 slow slip on the Superstition Hills Fault from Sentinel-1A Interferometric Synthetic Aperture Radar analysis. Positive values (red) correspond to motion away from the satellite. Quaternary faults are shown in gray (USGS, 2020). The locations of the creepmeters (yellow triangle) and Global Navigation Satellite System stations (red triangles) are also shown. Linear features oriented WNW-ESE are an artifact due to patch-wise filtering of the radar phase.

similar pattern (Wei et al., 2009, 2011), suggesting that some fraction of shallow creep may be accommodated by off-fault deformation (Fialko et al., 2005; Jin et al., 2022).

To evaluate the subsurface distribution of slip on the SHF due to the 2023 SSE, we performed kinematic inversions of the InSAR line-of-sight displacements (Figure 3) using an elastic halfspace dislocation model (see the Supporting Information for details). Our preferred slip model is shown in Figure 5 and features two primary asperities corresponding to the northern and southern sections of the SHF. Slip on the southern section is higher amplitude (>30 mm) and maximum at the surface, while slip on the northern section is more subdued (<20 mm) and has a maximum at depth of 1–2 km. The apparent "shallow slip deficit" (SSD) on the northern section of the SHF is likely an artifact of a distributed failure (Figure S3 in Supporting Information S1) that is not accounted for by our purely elastic model (Barbot et al., 2008; Lindsey, Sahakian, et al., 2014). The gap between the two slip patches corresponds to the step-over between the northern and southern SHF segments (Figures 1 and 3). Overall, slip is limited to the depth of sedimentary cover in the Imperial Valley (<4 km; Kohler & Fuis, 1986; Lindsey & Fialko, 2016; Wei et al., 2009). Converting the total slip from our preferred model (Figure 5) to moment magnitude, using shear modulus of 6 GPa ("The SCEC Unified Community Velocity Model Software Framework", 2017), we estimate that the 2023 SSE is equivalent to a M_w 4.5 earthquake, making it the largest documented SSE on the SHF to date (note that the moment magnitude of 4.7 for the 2006 event reported by Wei et al. (2009) was obtained assuming the shear modulus of 33 GPa, which is too high for the shallow sedimentary layer).

4. Discussion

The growing catalog of SSEs on the SHF enables a comparative analysis of the observed slip distributions. Each of the well-observed 2006, 2010, and 2023 SSEs is characterized by higher slip on the southern segment of the SHF, and lower slip on the northern segment (Figure 5). This spatial pattern was likely similar for the 1999 Hector Mine triggered slip, although the northern SHF was not mapped in-detail (perhaps due to the difficulty in finding

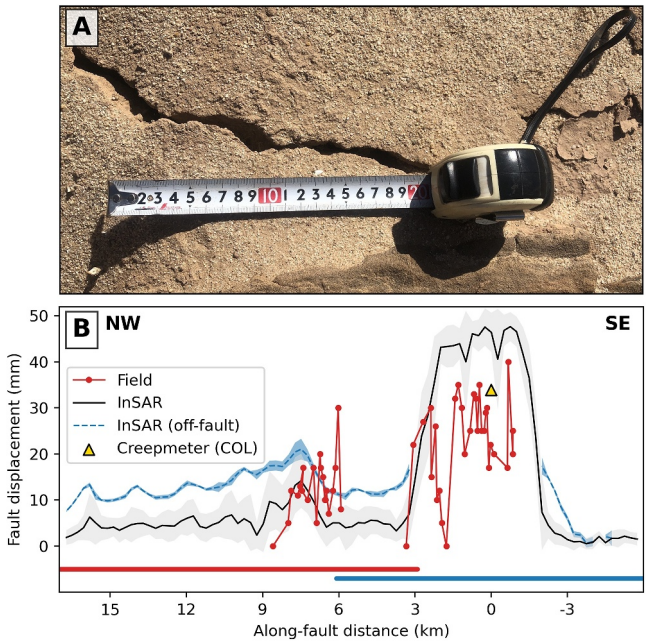

Figure 4. (a) An example surface crack observed during the 11 June 2023 field survey. The measuring tape is in centimeters and is aligned with the local strike. (b) 2023 Surface offsets along the Superstition Hills Fault (SHF). Estimated on-fault and maximum off-fault offsets from Interferometric Synthetic Aperture Radar (InSAR) are shown as solid black and dashed blue lines, respectively. Shaded areas denote estimated uncertainties. Red lines indicate offsets measured by field mapping. The COL creepmeter measurement is from 11 June, while InSAR displacements span 3 May to 8 June. Red and blue bars indicate the extent of the northern and southern SHF strands, respectively (Figure 1). Along-fault distances are referenced to the location of the creepmeters.

surface offsets in zones of distributed shear; Rymer et al., 2002). The respective ratios of slip amplitudes at the southern and northern fault sections are about 2:1 (Figure 3). Given that the entire fault appears to have slipped in the top few kilometers of the crust during the 2006, 2010, and 2023 SSEs (Figure 5; Wei et al., 2009; Wei et al., 2011), the largest SSEs occur as characteristic ruptures, with more strain release on the southern section of the SHF. This raises a question about the resulting relative surplus of strain on the northern SHF.

One possibility is that the systematic along-strike variations in surface slip (Figure 3) result from variations in the sediment thickness (Kohler & Fuis, 1986; Lindsey & Fialko, 2016; Wei et al., 2009) Assuming that shallow creep is limited to the sedimentary layer, the magnitude of surface slip is expected to scale with the sediment depth (e.g., Kaneko et al., 2013). In this case, lower slip during the interseismic period should be compensated by higher coseismic slip. However, the observed surface slip due to the 1989 Superstition Hills earthquake was essentially the same on the northern and southern sections of the SHF (Sharp et al., 1989). Another possibility is that the observed smaller slip on the northern SHF during "system-size" SSEs (Figures 3 and 5) is compensated by smaller SSEs that rupture only the northern SHF. There is some evidence for such events from the InSAR observations (Wei et al., 2015). The available data may not be sufficient to determine the average slip balance during the interseismic period, but it is clear that shallow creep on the SHF exhibits substantial spatio-temporal complexity, with both continuous and partial ruptures in the uppermost crust, heterogeneous slip distributions, variable near-surface slip localization, and rapid variations in slip rate (Figure 2). These features are not predicted by classic models of rate-state faults with the velocity-strengthening shallow layer (e.g., Kaneko et al., 2013; Li & Rice, 1987). Moreover, unlike the two most recent spontaneous SSEs (2006 and 2023) that were associated with slip durations of weeks, slip triggered by the El Major-Cucapah earthquake in 2010 was complete between two five-minute samples of the creepmeter. Previous models suggested that heterogeneity in frictional properties in the shallow crust may be responsible for the some of this behavior, for both spontaneous and triggered SSEs (Wei et al., 2015).

The interval between episodic SSEs following the 1987 earthquake has steadily increased from months to several years due to a decrease in the post-seismic stressing rate along shallow portion of the fault (Wei et al., 2013). These intervals are apparently shortened by the premature release of an accumulating SSD by shaking during major nearby earthquakes. For example, it is probable that the atypically abrupt surface slip induced by the 2010 El Major-Cucapah earthquake efficiently released a SSD that would otherwise have been accumulated and released within several years as a spontaneous SSE. The transition from rapid afterslip process to an episodic creep appears to have occurred starting 1995 ± 3 years, since when 15 cm of slip has been released in six SSEs. Afterslip presumably continues to contribute to surface slip because the intervals between episodic SSEs increases during these 28 years (i.e., shallow slip is not yet entirely attributable to the release of antiplane shear strain arising from interseismic deformation).

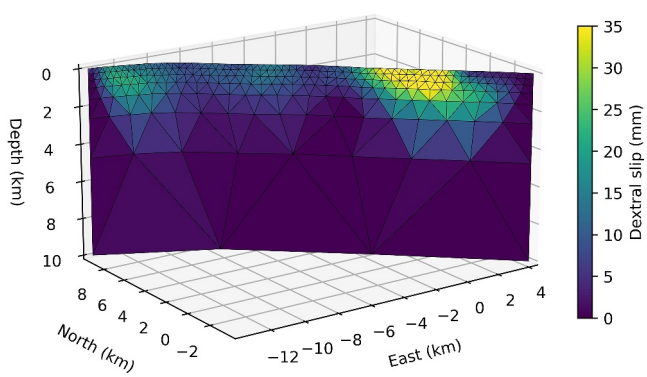

Figure 5. Three-dimensional kinematic model of slip on the Superstition Hills Fault during the 2023 slow-slip event. Fault patch colors correspond to the amplitude of dextral slip. The coordinates are centered at the location of the creepmeters. The moment release associated with this model corresponds to a M_w 4.5 earthquake.

From 2004 to May 2023, the averaged creep rate was 3.2 mm/yr (~5 mm/yr if including the 2023 SSE). The rate would be 3.2 mm/yr if we suppose that no spontaneous SSE occurs for a further decade, and 4.7 mm/yr should a ~40 mm event occur after this interval. These estimates are lower than the maximum long-term geological slip rate of 6 mm/yr adopted by Field et al. (2015), based largely on a 660 years geological slip rate of 2–6 mm/yr determined by Hudnut and Sieh (1989). However, the average shallow creep

rate should be a small fraction of the geologic slip rate, depending on the locking depths at the top and bottom of the seismogenic layer (e.g., Lindsey & Fialko, 2016). This implies a geologic slip rate on the SHF in excess of 10 mm/yr, higher than that assumed in the Uniform California Earthquake Rupture Forecast v.3 (UCERF3; Field et al., 2014), but consistent with the suggestion that the SHF is a continuation of the main strand of the San Jacinto fault with a slip rate of ∼15 mm/yr (Tymofyeyeva & Fialko, 2018; Vavra, Qiu, et al., 2023). While the duration of the post-seismic transient following the 1987 earthquake is not well known, the occurrence of SSEs in the late-interseismic period (Allen et al., 1972; Fuis, 1982; Rymer et al., 2002) suggests that both the average shallow creep rate and the long-term slip rate on the SHF are likely higher than assumed in the UCERF3 model.

5. Conclusions

We document the occurrence of a SSE (SSE) on the SHF which began in May 2023 and incremented in ≲5 mm sub-events, at uneven but increasing intervals for the following 60 days. InSAR measurements indicate the SSE likely initiated near the northern end of the fault and propagated ∼15 km to the south over the course of several days. Creepmeters on the southern SHF recorded up to 25 mm of dextral slip over the course of 3 days, with slip eventually attaining 41 mm by mid-July 2023. Fault offsets computed from InSAR data suggest maximum surface slip of 45+ mm. While slip is highly localized along a region of high slip on the southern end of the rupture, surface deformation along the northern ∼12 km of the fault is characterized by distributed shear over 400–1,300 m. Finite fault models derived from InSAR data indicate that the fault slip during the SSE was largest on the southern SHF. On the northern SHF, the average slip amplitude was lower by about a factor of two. Finite fault models also show that slip is largely confined to the shallowest 4 km of the fault, consistent with the depth of sediments and results inferred from previous SHF events. The moment release throughout the entire SSE sequence was equivalent to a $M_w \sim 4.5$ earthquake. The similarity of the 2023 SSE to previous events dating back to at least 2006 suggests spontaneous SSEs on the SHF have ruptured largely the same fault patches in a characteristic manner. Triggered slip induced by strong shaking from nearby earthquakes can both advance the timing of the release of an accumulating shallow slip deficit and reduce the duration of this slip from days to minutes.

Data Availability Statement

Raw Sentinel-1 data used in generating InSAR time series and velocity maps are openly available from Alaska Satellite Facility via https://search.asf.alaska.edu (ASF, 2022). Global Navigation Satellite System data are from the Earthscope Geodetic Facility for the Advancement of Geoscience Data Center via https://www.unavco.org/data/gps-gnss/gps-gnss.html (EarthScope, 2022). Processed geodetic and field data used in this study are available via Zenodo (https://zenodo.org/records/10211682; Vavra, Fialko, et al., 2023). The seismicity catalogs are available from the Southern California Earthquake Center via https://scedc.caltech.edu/data (SCEDC, 2013).

Acknowledgments
We thank Editor Germán Prieto and two anonymous reviewers for feedback that helped improve this article. We also thank Kathryn Materna for thoughtful and engaging discussions regarding the 2023 SHF event. Funding for this study was provided by NSF (GRFP to EV, EAR-1841273 to YF) and NASA (80NSSC22K0506 to YF). YF acknowledges High-End Computing resources from NASA. Funding from USGS and NASA have supported creepmeter maintenance. PS, JaS, PT, and JoS gratefully acknowledge support from the research program "Strategy AV21 Dynamic Planet Earth" and greatly appreciate institutional support from the IRSM CAS (Long-Term Conceptual Development of the Research Organisation, RVO: 67985891).

References

Allen, C. R., Wyss, M., Brune, J. N., Grantz, A., & Wallace, R. E. (1972). Displacements on the Imperial, Superstition Hills, and San Andreas faults triggered by the Borrego mountain earthquake. Geological Survey Professional Paper. No. 787, 87–104.

ASF. (2022). European Space Agency Copernicus Sentinel data [Dataset]. *Alaska Satellite Facility Distributed Active Archive Center*. https://search.asf.alaska.edu/

Barbot, S., Fialko, Y., & Bock, Y. (2009). Postseismic deformation due to the M_w 6.0 2004 Parkfield earthquake: Stress-driven creep on a fault with spatially variable rate-and-state friction parameters. *Journal of Geophysical Research*, *114*(B7), B07405. https://doi.org/10.1029/2008jb005748

Barbot, S., Fialko, Y., & Sandwell, D. (2008). Effect of a compliant fault zone on the inferred earthquake slip distribution. *Journal of Geophysical Research*, *113*(B6), B06404. https://doi.org/10.1029/2007jb005256

Bilham, R. (1989). Surface slip subsequent to the 24 November 1987 Superstition Hills, California, earthquake monitored by digital creepmeters. *Bulletin of the Seismological Society of America*, *79*(2), 424–450.

Bilham, R., & Castillo, B. (2020). The July 2019 Ridgecrest, California, earthquake sequence recorded by creepmeters: Negligible epicentral afterslip and prolonged triggered slip at teleseismic distances. *Seismological Research Letters*, *91*(2A), 707–720. https://doi.org/10.1785/0220190293

Bodin, P., Bilham, R., Behr, J., Gomberg, J., & Hudnut, K. (1994). Slip triggered on southern California faults by the 1992 Joshua Tree, Landers, and Big Bear earthquakes. *Bulletin of the Seismological Society of America*, *84*, 806–816.

Brooks, B. A., Minson, S. E., Glennie, C. L., Nevitt, J. M., Dawson, T., Rubin, R., et al. (2017). Buried shallow fault slip from the South Napa earthquake revealed by near-field geodesy. *Science Advances*, *3*(7), e1700525. https://doi.org/10.1126/sciadv.1700525

Donnellan, A., Parker, J., Hensley, S., Pierce, M., Wang, J., & Rundle, J. (2014). UAVSAR observations of triggered slip on the Imperial, Superstition Hills, and east Elmore Ranch faults associated with the 2010 M 7.2 El Mayor-Cucapah earthquake. *Geochemistry, Geophysics, Geosystems*, *15*(3), 815–829. https://doi.org/10.1002/2013gc005120

Dragert, H., Wang, K., & James, T. S. (2001). A silent slip event on the Deeper Cascadia subduction interface. *Science*, *292*(5521), 1525–1528. https://doi.org/10.1126/science.1060152

EarthScope. (2022). Global navigation satellite system position solutions [Dataset]. *Geodetic Facility for the Advancement of Geoscience*. https://www.unavco.org/data/gps-gnss/gps-gnss.html

Fialko, Y. (2006). Interseismic strain accumulation and the earthquake potential on the southern San Andreas fault system. *Nature*, *441*(7096), 968–971. https://doi.org/10.1038/nature04797

Fialko, Y., Sandwell, D., Agnew, D., Simons, M., Shearer, P., & Minster, B. (2002). Deformation on nearby faults induced by the 1999 Hector Mine earthquake. *Science*, *297*(5588), 1858–1862. https://doi.org/10.1126/science.1074671

Fialko, Y., Sandwell, D., Simons, M., & Rosen, P. (2005). Three-dimensional deformation caused by the Bam, Iran, earthquake and the origin of shallow slip deficit. *Nature*, *435*(7040), 295–299. https://doi.org/10.1038/nature03425

Field, E. H., Arrowsmith, R. J., Biasi, G. P., Bird, P., Dawson, T. E., Felzer, K. R., et al. (2014). Uniform California earthquake rupture Forecast, version 3 (UCERF3) the time-independent model. *Bulletin of the Seismological Society of America*, *104*, 1122–1180. https://doi.org/10.1785/0120130164

Field, E. H., Biasi, G. P., Bird, P., Dawson, T. E., Felzer, K. R., Jackson, D. D., et al. (2015). Long-term time-dependent probabilities for the third Uniform California earthquake rupture Forecast (UCERF3). *Bulletin of the Seismological Society of America*, *105*(2A), 511–543. https://doi.org/10.1785/0120140093

Fuis, G. S. (1982). *Displacement on the Superstition Hills fault triggered by the earthquake* (Vol. 1254, pp. 145–154). U.S. Geologic Survey Professional Paper.

Hauksson, E., Stock, J., Bilham, R., Boese, M., Chen, X., Fielding, E. J., et al. (2013). Report on the August 2012 Brawley earthquake swarm in Imperial Valley, Southern California. *Seismological Research Letters*, *84*(2), 177–189. https://doi.org/10.1785/0220120169

Heflin, M., Donnellan, A., Parker, J., Lyzenga, G., Moore, A., Ludwig, L. G., et al. (2020). Automated estimation and tools to extract positions, velocities, breaks, and seasonal terms from daily GNSS measurements: Illuminating nonlinear Salton Trough deformation. *Earth and Space Science*, *7*(7), e2019EA000644. https://doi.org/10.1029/2019ea000644

Hudnut, K. W., & Sieh, K. E. (1989). Behavior of the Superstition Hills fault during the past 330 years. *Bulletin of the Seismological Society of America*, *79*(2), 304–329.

Jin, Z., Fialko, Y., Zubovich, A., & Schöne, T. (2022). Lithospheric deformation due to the 2015 M7.2 Sarez (Pamir) earthquake constrained by 5 years of space geodetic observations. *Journal of Geophysical Research: Solid Earth*, *127*(4), e2021JB022461. https://doi.org/10.1029/2021jb022461

Kaneko, Y., Fialko, Y., Sandwell, D. T., Tong, X., & Furuya, M. (2013). Interseismic deformation and creep along the central section of the north Anatolian fault (Turkey): InSAR observations and implications for rate-and-state friction properties. *Journal of Geophysical Research: Solid Earth*, *118*(1), 316–331. https://doi.org/10.1029/2012jb009661

Klimeš, J., Rowberry, M. D., Blahůt, J., Briestenský, M., Hartvich, F., Košťák, B., et al. (2012). The monitoring of slow-moving landslides and assessment of stabilisation measures using an optical–mechanical crack gauge. *Landslides*, *9*(3), 407–415. https://doi.org/10.1007/s10346-011-0306-4

Kohler, W. M., & Fuis, G. S. (1986). Travel-time, time-term, and basement depth maps for the Imperial Valley region, California, from explosions. *Bulletin of the Seismological Society of America*, *76*(5), 1289–1303.

Košťák, B. (1969). A new device for in-situ movement detection and measurement. *Experimental Mechanics*, *9*(8), 374–379. https://doi.org/10.1007/bf02327715

LaBonte, A., Brown, K., & Fialko, Y. (2009). Hydrogeologic detection and finite-element modeling of a slow-slip event in the Costa Rica prism toe. *Journal of Geophysical Research*, *114*(B4), B00A02. https://doi.org/10.1029/2008jb005806

Li, V. C., & Rice, J. (1987). Crustal deformation in great California earthquake cycles. *Journal of Geophysical Research*, *92*(B11), 11533–11551. https://doi.org/10.1029/jb092ib11p11533

Lindsey, E. O., & Fialko, Y. (2016). Geodetic constraints on frictional properties and earthquake hazard in the Imperial Valley, southern California. *Journal of Geophysical Research: Solid Earth*, *121*(2), 1097–1113. https://doi.org/10.1002/2015jb012516

Lindsey, E. O., Fialko, Y., Bock, Y., Sandwell, D. T., & Bilham, R. (2014). Localized and distributed creep along the southern San Andreas fault. *Journal of Geophysical Research: Solid Earth*, *119*(10), 7909–7922. https://doi.org/10.1002/2014jb011275

Lindsey, E. O., Sahakian, V. J., Fialko, Y., Bock, Y., Barbot, S., & Rockwell, T. K. (2014). Interseismic strain localization in the San Jacinto fault zone. *Pure and Applied Geophysics*, *171*(11), 2937–2954. https://doi.org/10.1007/s00024-013-0753-z

Louie, J. N., Johnson, D. C., Haase, P. C., & Cohn, S. N. (1985). Fault slip in southern California. *Bulletin of the Seismological Society of America*, *75*(3), 811–833. https://doi.org/10.1785/bssa0750030811

Marone, C., Scholz, C., & Bilham, R. (1991). On the mechanics of earthquake afterslip. *Journal of Geophysical Research*, *96*(B5), 8441–8452. https://doi.org/10.1029/91jb00275

Martí, X., Rowberry, M. D., & Blahůt, J. (2013). A MATLAB® code for counting the moiré interference fringes recorded by the optical-mechanical crack gauge TM-71. *Computers and Geosciences*, *52*, 164–167. https://doi.org/10.1016/j.cageo.2012.09.029

Nof, R. N., Ziv, A., Doin, M.-P., Baer, G., Fialko, Y., Wdowinski, S., et al. (2012). Rising of the lowest place on Earth due to Dead Sea water-level drop: Evidence from SAR interferometry and GPS. *Journal of Geophysical Research*, *117*(B5). https://doi.org/10.1029/2011jb008961

Parker, J., Donnellan, A., Bilham, R., Ludwig, L. G., Wang, J., Pierce, M., et al. (2021). Buried aseismic slip and off-fault deformation on the southernmost San Andreas fault triggered by the 2010 El Mayor Cucapah earthquake revealed by UAVSAR. *Earth and Space Science*, *8*(8). https://doi.org/10.1029/2021ea001682

Pearse, J., & Fialko, Y. (2010). Mechanics of active magmatic intraplating in the Rio Grande rift near Socorro, New Mexico. *Journal of Geophysical Research*, *115*(B7), B07413. https://doi.org/10.1029/2009jb006592

Ross, Z. E., Trugman, D. T., Hauksson, E., & Shearer, P. M. (2019). Searching for hidden earthquakes in southern California. *Science*, *364*(6442), 767–771. https://doi.org/10.1126/science.aaw6888

Rymer, M. J. (2000). Triggered surface slips in the Coachella Valley area associated with the 1992 Joshua Tree and Landers, California, earthquakes. *Bulletin of the Seismological Society of America*, *90*(4), 832–848. https://doi.org/10.1785/0119980130

Rymer, M. J., Boatwright, J., Seekins, L. C., Yule, D., & Liu, J. (2002). Triggered surface slips in the Salton Trough associated with the 1999 Hector Mine, California, earthquake. *Bulletin of the Seismological Society of America*, *92*(4), 1300–1317. https://doi.org/10.1785/0120000935

SCEDC. (2013). Southern California earthquake data center [Dataset]. *Caltech*. https://doi.org/10.7909/C3WD3XH1

Sharp, R. V. (1967). San Jacinto fault zone in the peninsular ranges of southern California. *Geological Society of America Bulletin*, *78*(6), 705–730. https://doi.org/10.1130/0016-7606(1967)78[705:sjfzit]2.0.co;2

Sharp, R. V., Budding, K. E., Boatwright, J., Ader, M. J., Bonilla, M. G., Clark, M. M., et al. (1989). Surface faulting along the Superstition Hills fault zone and nearby faults associated with the earthquakes of 24 November 1987. *Bulletin of the Seismological Society of America*, *79*(2), 252–281. https://doi.org/10.1785/bssa0790020252

Sharp, R. V., Rymer, M. J., & Lienkaemper, J. J. (1986). Surface isplacement on the imperial and superstition hills faults triggered by the Westmoreland, California, earthquake 26 April 1981. *Bulletin of the Seismological Society of America*, *76*(4), 949–965. https://doi.org/10.1785/bssa0760040949

Shaw, J. H., Plesch, A., Tape, C., Suess, M. P., Jordan, T. H., Ely, G., et al. (2015). Unified structural representation of the southern California crust and upper mantle. *Earth and Planetary Science Letters*, *415*, 1–15. https://doi.org/10.1016/j.epsl.2015.01.016

Small, P., Gill, D., Maechling, P. J., Taborda, R., Callaghan, S., Jordan, T. H., et al. (2017). The SCEC unified community velocity model software framework. *Seismological Research Letters*, *88*(6), 1539–1552. https://doi.org/10.1785/0220170082

Tymofyeyeva, E., & Fialko, Y. (2015). Mitigation of atmospheric phase delays in InSAR data, with application to the eastern California shear zone. *Journal of Geophysical Research: Solid Earth*, *120*(8), 5952–5963. https://doi.org/10.1002/2015jb011886

Tymofyeyeva, E., & Fialko, Y. (2018). Geodetic evidence for a blind fault segment at the southern end of the San Jacinto fault zone. *Journal of Geophysical Research: Solid Earth*, *123*(1), 878–891. https://doi.org/10.1002/2017jb014477

Tymofyeyeva, E., Fialko, Y., Jiang, J., Xu, X., Sandwell, D., Bilham, R., et al. (2019). Slow slip event on the southern San Andreas fault triggered by the 2017 M_w 8.2 Chiapas (Mexico) earthquake. *Journal of Geophysical Research: Solid Earth*, *124*(9), 9956–9975. https://doi.org/10.1029/2018jb016765

USGS. (2020). *Quaternary Fault and fold database for the Nation*. USGS.

Vavra, E. J., Fialko, Y., Bilham, R., Rockwell, Å. P., Thomas, Stemberk, J., et al. (2023). Measurements of fault slip associated with the 2023 Superstition Hills fault slow slip event [Dataset]. *Zenodo*. https://doi.org/10.5281/zenodo.10211681

Vavra, E. J., Qiu, H., Chi, B., Share, P.-E., Allam, A., Morzfeld, M., et al. (2023). Active dipping interface of the southern San Andreas fault revealed by space geodetic and seismic imaging. *Journal of Geophysical Research: Solid Earth*, *128*(11), e2023JB026811. https://doi.org/10.1029/2023jb026811

Wald, D. J., Helmberger, D. V., & Hartzell, S. H. (1990). Rupture process of the 1987 Superstition Hills earthquake from the inversion of strong-motion data. *Bulletin of the Seismological Society of America*, *80*(5), 1079–1098. https://doi.org/10.1785/bssa0800051079

Wallace, L. M. (2020). Slow slip events in New Zealand. *Annual Review of Earth and Planetary Sciences*, *48*(1), 175–203. https://doi.org/10.1146/annurev-earth-071719-055104

Wei, M., Kaneko, Y., Liu, Y., & McGuire, J. J. (2013). Episodic fault creep events in California controlled by shallow frictional heterogeneity. *Nature Geoscience*, *6*(7), 566–570. https://doi.org/10.1038/ngeo1835

Wei, M., Liu, Y., Kaneko, Y., McGuire, J. J., & Bilham, R. (2015). Dynamic triggering of creep events in the Salton Trough, southern California by regional M ≥ 5.4 earthquakes constrained by geodetic observations and numerical simulations. *Earth and Planetary Science Letters*, *427*, 1–10. https://doi.org/10.1016/j.epsl.2015.06.044

Wei, M., Sandwell, D., & Fialko, Y. (2009). A silent M_w 4.7 slip event of October 2006 on the Superstition Hills fault, southern California. *Journal of Geophysical Research*, *114*(B7), B07402. https://doi.org/10.1029/2008jb006135

Wei, M., Sandwell, D., Fialko, Y., & Bilham, R. (2011). Slip on faults in the Imperial Valley triggered by the 4 April 2010 M_w 7.2 El Mayor-Cucapah earthquake revealed by InSAR. *Geophysical Research Letters*, *38*(1). https://doi.org/10.1029/2010gl045235

Williams, P. L., & Magistrale, H. W. (1989). Slip along the superstition Hills Fault associated with the 24 November 1987 Superstition Hills, California, earthquake. *Bulletin of the Seismological Society of America*, *79*(2), 390–410.

Zebker, H. A., Rosen, P. A., & Hensley, S. (1997). Atmospheric effects in interferometric synthetic aperture radar surface deformation and topographic maps. *Journal of Geophysical Research*, *102*(B4), 7547–7563. https://doi.org/10.1029/96jb03804

References From the Supporting Information

Aster, R. C., Borchers, B., & Thurber, C. H. (2018). *Parameter estimation and inverse problems*. Elsevier.

Brodsky, E. E., Roeloffs, E., Woodcock, D., Gall, I., & Manga, M. (2003). A mechanism for sustained groundwater pressure changes induced by distant earthquakes. *Journal of Geophysical Research*, *108*(B8), 2390. https://doi.org/10.1029/2002jb002321

Emardson, T. R., Simons, M., & Webb, F. H. (2003). Neutral atmospheric delay in interferometric synthetic aperture radar applications: Statistical description and mitigation (p. 108).

Jonsson, S. (2002). Fault slip distribution of the 1999 M_w 7.1 Hector Mine, California, earthquake, estimated from satellite radar and GPS measurements. *Bulletin of the Seismological Society of America*, *92*(4), 1377–1389. https://doi.org/10.1785/0120000922

Kostak, B., & Popp, K. (1966). Moiré strain gauges. *Strain*, *2*(2), 5–16. https://doi.org/10.1111/j.1475-1305.1966.tb00490.x

Lohman, R. B., & Simons, M. (2005). Some thoughts on the use of InSAR data to constrain models of surface deformation: Noise structure and data downsampling. *Geochemistry, Geophysics, Geosystems*, *6*(1). https://doi.org/10.1029/2004gc000841

Nikkhoo, M., & Walter, T. R. (2015). Triangular dislocation: An analytical, artefact-free solution. *Geophysical Journal International*, *201*(2), 1119–1141. https://doi.org/10.1093/gji/ggv035

Segall, P. (2010). *Earthquake and volcano deformation*. Princeton University Press.

Simons, M. (2002). Coseismic deformation from the 1999 M_w 7.1 Hector Mine, California, earthquake as inferred from InSAR and GPS observations. *Bulletin of the Seismological Society of America*, *92*(4), 1390–1402. https://doi.org/10.1785/0120000933

Wang, K., & Fialko, Y. (2018). Observations and modeling of co- and postseismic deformation due to the 2015 M_w 7.8 Gorkha (Nepal) earthquake. *Journal of Geophysical Research*, *123*(1), 761–779. https://doi.org/10.1002/2017jb014620